ELSEVIER

Spectrochimica Acta Part B 63 (2008) 257–270

SPECTROCHIMICA ACTA PART B

www.elsevier.com/locate/sab

Design analysis of a laser ablation cell for inductively coupled plasma mass spectrometry by numerical simulation ☆

D. Autrique [a,*], A. Bogaerts [a], H. Lindner [b], C.C. Garcia [b], K. Niemax [b]

[a] *University of Antwerp, Department of Chemistry, Research Group for Plasma, Laser Ablation and Surface Modelling — Antwerp (PLASMANT), Universiteitsplein 1, B-2610 Wilrijk, Belgium*

[b] *ISAS— Institute for Analytical Sciences, University of Dortmund, Bunsen-Kirchhoff-Strasse 11, D-44139 Dortmund, Germany*

Received 13 October 2007; accepted 23 November 2007
Available online 4 December 2007

Abstract

A laser ablation setup including outer chamber, sample tube, sample holder and transport tubing was modelled and optimized using advanced computational fluid dynamics techniques. The different components of the setup were coupled and the whole device was modelled at once. The mass transport efficiency and transit times of near infrared femtosecond (fs) laser generated brass aerosols in pure argon and helium–argon mixtures were calculated at experimentally optimized conditions and a transient signal was constructed. The use of helium or argon did not influence the mass transport efficiency, but the signal structure changed. The signal fine structure was retrieved and experimentally validated. Bimodal peak structures were observed that seemed to originate from turbulent effects in the tubing connecting a Y-connector and the injector.

Keywords: Laser ablation; Aerosol transport; Numerical simulation; Inductively coupled plasma mass spectrometry

1. Introduction

1.1. Background

Direct solid microanalysis using laser ablation (LA) in combination with inductively coupled plasma mass spectrometry (ICP-MS) is nowadays one of the most frequently used techniques for a fast and powerful multi-element determination of solid samples at the trace and ultra-trace concentration levels of a wide variety of sample types [1–11].

The growing interest in LA as a sample introduction technique stems from the ability to sample diverse materials ranging from conducting to non-conducting inorganic and organic compounds as solids or powders. Besides bulk analysis, the focussing characteristics of lasers permit sampling in small areas, so that localized microanalysis and spatially resolved studies are feasible.

The first application of the use of LA for sample introduction into ICP-MS was reported by Gray [12], who used a ruby laser to vaporize portions of solid samples prior to transport to the plasma for ionization. His work is distinct from Laser Microprobe Mass Spectrometry (LMMS), in which the laser beam is used both to extract sample atoms from a solid and to ionize them. The essential differences are that in LA-ICP-MS the sample remains at atmospheric pressure instead at vacuum conditions and ionization is performed separately from LA in a second step in the ICP, thus permitting separate optimization of two successive processes.

In order to combine LA with ICP excitation or ionization, the sample is setup in a chamber. Material is ablated from the sample and particles are formed. These particles are then transported to the plasma for atomization and ionization. An aerosol carrier gas is passed through the cell at a constant flow rate and directed through the plumbing system to the injector tube in the plasma torch.

During the LA-ICP-MS measurement, the ablation chamber geometry and the connective transport tubing play an important role. They affect the overall transport efficiency and the measured signal profile. The whole setup should be constructed in

☆ This article is published in a special honor issue dedicated to Jim Winefordner on the occasion of his retirement, in recognition of his outstanding accomplishments in analytical atomic and molecular spectroscopy.

* Corresponding author. Tel.: +32 3 820 23 83; fax: +32 3 820 23 76.
E-mail address: david.autrique@ua.ac.be (D. Autrique).

0584-8547/$ - see front matter © 2007 Elsevier B.V. All rights reserved.
doi:10.1016/j.sab.2007.11.032

such a way that the aerosol loss is minimized and should allow rapid transport from the ablation site to the ICP source.

In the 80's, Moenke–Blankenburg and coworkers [13,14] performed some interesting experiments on the effect of setup geometry on the inductively coupled plasma optical emission spectroscopy (ICP-OES) signal profile. They demonstrated the influence of the volume of the ablation cell and the influence of the tube length/diameter on the signal dispersion. Based on their experimental findings a theoretical analytical model was developed. Moreover they implemented a single bead string reactor (SBSR) in their tubing, in order to minimize signal dispersion. This concept, adapted from flow-injection analysis [15], leads to sharper signals as compared with the free tube transport condition.

Leach and Hieftje [16] investigated experimentally the effects on transient signal profiles by varying the ablation cell volume, the diameter and the length of the transfer tube and the composition and flow rate of the ablation cell sweep gases. They observed that minimization of the cell volume and the length and diameter of the transfer tube dramatically decreased the peak width of the transient signals. Furthermore, they reported that the use of helium carrier gas also drastically decreased the peak width of transient signals.

Bleiner and Günther [17,18] studied experimentally the effect of setup geometry on single shot characteristics in combination with ICP-MS. Moreover, they developed a theoretical analytical description for the effect of setup geometry on the signal characteristics. Their theoretical relation was based on a product of a cell-related elution function and a tube-filling function [6–8], assuming laminar flow in the transfer line and ideal mixing in the ablation cell. The study showed that the ablation cell volume and shape influenced the signal structure most notably. Moreover they reported that the mass transport efficiency for cells up to 100 cm^3 could be maintained under different transport conditions.

Plotnikov [19], however, noted that the form of their function deviated from the experimental data. He suggested a new response curve without detailed consideration of the physical meaning of all the parameters of the function.

Recently, some other analytical transport models were proposed for the LA-ICP-MS temporal intensity distribution. Gäckle and Mertens [20,21] modelled the temporal intensity distribution in LA-ICP-MS by means of single shot, scanning and drilling mode.

Koch et al. [22] suggested the use of computational fluid dynamics (CFD) in order to describe the transport characteristics of ablation cells in a quantitative way.

In 2006, Bleiner and Bogaerts [23] presented the first systematic numerical investigations on the effect of laser ablation setup on the ns-LA-ICP-MS profile by means of CFD. The performance of several sample chambers was studied later on [24]. Compared to previous models, they considered the particle size as a variable in their calculations and investigated its effects on the transport efficiency and signal characteristics. It was demonstrated that the use of junction or barriers such as the SBSR in the tubing could perturb and deteriorate the transport efficiency. Moreover it appeared that a strict laminar condition in the tubing as stated in [20,21] was not valid; the threshold velocity for turbulence onset in their model was as low as 2% of the speed of sound. Finally they completed the findings of [19] by an in-depth physical study of the signal profile and demonstrated the lack of mass conservation in the previous models.

The models summarized above, described the temporal intensity distribution based on analytical expressions. The attractive aspect of this approach is the fact that similar calculations can be repeated in a fast and straightforward way. Besides they were helpful in retrieving the characteristics of ablation setups.

From a theoretical point of view, however, this approach is not suitable for predicting the signal fine structure, nor the correct signal profile since it is based on mean flow properties and since it disregards the highly non-linear physical processes that influence the overall signal intensity.

In order to improve and design ablation setups and in order to reconstruct an ICP-MS signal theoretically, it is expedient to use pure numerical approaches. Nevertheless, one should realize that no model will ever be able to predict the exact temporal intensity, due to the simple fact that every model has its limitations.

1.2. Aim of the study

The aim of this work is to investigate an ablation setup as has been used in [25] by means of CFD simulations. The mass transport efficiency and transit times of near infrared femtosecond (fs) laser generated brass aerosols in pure argon and helium–argon mixtures will be calculated and a transient signal will be constructed. Based on the modelled flow and signal patterns, the weaknesses of the ablation setup will be detected. Accordingly, future theoretical work would then focus on the further optimization of the present design by removing the detected drawbacks, changing the flow rates and ablation cell dimensions and finally lead to a fully optimized cell.

1.3. Why using CFD?

Computational fluid dynamics constitutes a new third approach in the philosophical study and development of the whole discipline of fluid dynamics. In the 17th century the foundations of experimental fluid dynamics were laid, the 18th and 19th century saw gradually the development of theoretical fluid dynamics. The advent of high-speed computers combined with the development of accurate numerical algorithms for solving physical problems has revolutionized the way we study and practice fluid dynamics today.

Although many of the key ideas for numerical solution methods for partial differential equations were established more than a century ago, they were of little use before computers appeared. While the first computers built in the 1950's performed only a few hundred operations per second, machines are now being designed to produce teraflops i.e., 10^{12}-floating operations per second.

It requires little imagination to see that computers might make the study of fluid flow easier and more effective. Once the power of computers has been recognized, interest in numerical

techniques increased dramatically. Solution of the equations of fluid mechanics on computers has become so important that it now occupies the attention of a third of the fluid mechanics community, meanwhile the proportion is still increasing.

However, to keep things in perspective, computational fluid dynamics provides a new third scientific approach, but it will never replace the other two. It rather complements the other approaches of pure theory and pure experiment.

It is a tool that can be used for instance to obtain a deeper insight in experimental results and to optimize experimental designs. The variable cost of an experiment, in terms of facility hire and man-hour costs, is proportional to the number of data points and the number of cell-configurations tested. In contrast, CFD codes can produce large numbers of results at virtually no added expense and it is very cheap to perform parametric studies, for instance to optimize equipment performance.

In this case, computer simulations of aerosol particle introduction for a specific laser sampling system were used to determine the optimum geometry of a specific ablation setup.

1.4. Strategy of the present study

The flow pattern and particle transport in an ablation setup can be described by partial differential equations or integro-differential equations, which cannot be solved analytically except in special cases. To obtain an approximate solution numerically, one must use a discretization method which approximates the differential equations by a system of algebraic equations, that can be solved on a computer. The approximations are applied to small domains in space and time so that the numerical solution provides results at discrete locations in space and time.

Accordingly most commercial CFD packages contain two main elements: a pre-processor and a solver.

Pre-processing involves:

1. Specification of the computational domain. In our case this means the construction of a geometrically and topologically consistent equivalent of the ablation setup.
2. Sub-division of the domain into a number of smaller non-overlapping sub-domains: as a result a grid, containing many control volumes is constructed.
3. Specification of appropriate boundary conditions as flow rate, temperature, ambient pressure, flow gas mass fractions, etc.

The solver-part includes the following steps:

1. Discretization of the governing flow equations.
2. Solution of the algebraic equations. Due to the fact that the governing fluid equations were non-linear, iterative matrix solvers were applied.

While the accuracy of experimental results depends on the quality of the tools and operator capability, the accuracy of numerical solutions is dependent on the applied discretization schemes and grid quality. There is danger that erroneous solutions may look good, but may not correspond to the actual boundary conditions and fluid properties. In case the mathematical underground of CFD has been disregarded, incorrectly calculated flow features, that could be interpreted as physical phenomena, are produced. Even in case that commercial CFD packages are used, this type of problems persist. For that reason 60% of the time spent on the CFD project was devoted to the definition of the domain geometry, grid generation and discretization techniques.

Compared to the numerical models described above [22–24], the whole ablation setup was modelled at once in the present study, including the outer box, sample tube, sample holder and the tubing connecting the ablation cell and the injector to the ICP. The CFD simulations were conducted by means of a *Gambit*/*Fluent* software and the *C*-programming language.

2. Theory

2.1. Turbulence

As has been pointed out in [22,25–28], the flow pattern in ablation setups can be turbulent. The onset for turbulent flow is mostly described in terms of the magnitude ratio of inertial and viscous forces. This ratio, called the Reynolds number, can be expressed as $Re=\rho UL/\mu$, with ρ the fluid density, μ the viscosity, U the *averaged* reference velocity and L the reference length. Experiments have been conducted using a wide variety of fluids in pipes of various diameters that confirm that Reynolds numbers characterize the velocity of the flow wherein laminar flow breaks into turbulent flow. At $Re \leq 2000$ the flow in a smooth-surfaced pipe is always laminar. For $2000 < Re < 4000$ there is a gradual change to turbulence. For $Re > 4000$, the flow is customarily considered turbulent, though portions of the flow may still remain laminar.

If there are protrusions in the flow, it may trip into turbulence at a lower Reynolds number.

Turbulence can cause deterioration in time-dependent sample introduction [25–27], and can be regarded as a negative event. This is probably the main cause for the experimental observed irreproducible, fluctuating, splitted signal peaks [25–27].

In other cases turbulence is considered as a positive event, that can be used to improve and homogenize the LA-ICP-MS signal characteristics [13,14,28].

Since the particle size distribution produced under fs-pulsed irradiation is much finer than the one produced by ns-pulsed lasers, the width of the fs-signals is much smaller compared to ns-signals. So the mixing characteristics of turbulence (see below: Section 2.2.) are of little value in case of fs-ablation.

As will be shown in the next paragraphs, turbulence would just deteriorate the fs-signals and should be avoided in fs-ablation setups. As stated in ref. [26], the conditions for turbulence in ICP-MS sample chambers are practically always met. We will demonstrate that this is also the case for the tubing that was used in ref. [25].

2.2. Characteristics of turbulence

If we would consider laminar flow in a constant diameter tube, we could view the motion of fluid as consisting of steadily

advancing layers of fluid. In case we would increase the flow rate, which results in an increase of the Reynolds number, we would observe the flow becoming unsteady with slugs of fluid superimposed on the main flow moving in a rather chaotic fashion. The flow became turbulent.

The inherent requirement for the existence of turbulence is shear. Turbulence is the result of viscosity, but in a subtle way. As viscosity dampens out turbulence and is one of the factors that makes a flow "well behaved", it cannot by itself make turbulence. Turbulence is made by surface friction, which is a local phenomenon, so it is not spread out like laminar friction. Near the surface of the tube, shear stresses slow the fluid down, creating large velocity gradients. If the velocity gradient is large enough, the local surface friction transforms the fluid into small eddies. Some of these eddies are transported to the centre of the pipe where they combine with other eddies to form larger ones. The result of these processes is a turbulent flow, characterized by fluctuating velocity fields. These fluctuations mix transported quantities such as momentum, energy, and species concentration, and cause the transported quantities to fluctuate as well.

The evolution of turbulent flows is very complex. Turbulent flows appear highly disorganized with structure at all scales. So the LA-ICP-MS signals appear to be unpredictable in their detailed behaviour. However, some statistical properties of the flow can be quite reproducible. This suggests that it can be useful to seek a statistical description of turbulent flows. A statistical measure is an average of some kind: over the symmetry coordinates, if any are available (e.g. a time average for stationary flows); over multiple realizations (e.g. an ensemble); or over the phase space of solutions if the dynamics are homogeneous.

Thus it seems quite appropriate to introduce a probabilistic description of turbulence. However, we know that the basic fluid equations are deterministic. How can chance and chaos arise in a purely deterministic context? Ilya Prigogine [29,30] has in recent years brought about a radical change of perspective. The statistical description of turbulence is not merely a convenience to describe the excessive amount of information contained in the fluid. Turbulence is intrinsically stochastic. The argument goes that single trajectories of fluid parcels in phase space are deterministic, but a fluid composed by a large ensemble of parcels is not. All parcels interact in such a way that information is continuously spread, and the ensemble evolves toward a collective state that can be defined only statistically. This description suggests that irreversibility appears in nature as a result of the statistical behaviour of parcel interactions [31].

3. Description of the model

The most accurate approach to turbulence simulation is to solve the Navier–Stokes equations without averaging or approximation other than numerical discretizations, whose errors can be estimated and controlled. It is also the simplest approach from a conceptual point of view, that is able to resolve all the motions that are contained in the flow. The problem, however, is that this approach, called Direct Numerical Simulation (DNS), is computationally too expensive [32]. Instead the instantaneous, exact governing equations can be time-averaged or ensemble-averaged (see Section 2.2. above), resulting in a modified set of equations that are less expensive to solve: the Reynolds-Averaged Navier-Stokes (RANS) equations, as will be presented in the next section [33].

3.1. Time-averaged fluid equations

In Reynolds averaging the solution variables in the exact Navier–Stokes equations are decomposed into mean and fluctuating components. For instance velocity components are decomposed as: $u_i=\overline{u_i}+u_i$' where $\overline{u_i}$ and u_i' are the mean and fluctuating components, respectively.

The time-averaged continuity and momentum equations can then be written in Cartesian tensor form as:

$$\frac{\partial \rho}{\partial t}+\frac{\partial}{\partial x_i}(\rho u_i)=0 \tag{1}$$

$$\frac{\partial}{\partial t}(\rho u_i)+\frac{\partial}{\partial x_j}(\rho u_i u_j)=-\frac{\partial p}{\partial x_i}+\frac{\partial}{\partial x_j} \times\left[\mu\left(\frac{\partial u_i}{\partial x_j}+\frac{\partial u_j}{\partial x_i}-\frac{2}{3}\delta_{ij}\frac{\partial u_l}{\partial x_l}\right)\right]-\frac{\partial}{\partial x_j}\left(p\,\overline{u_i' u_j'}\right) \tag{2}$$

where ρ denotes the mass density, p is the pressure. u_i, u_i' and x_i are the mean velocity components, fluctuating velocity components and the spatial coordinates, respectively (i, j, l=1,2,3).

The exact Navier–Stokes equations form a closed set of four equations with four unknowns. In contrast, in performing the time-averaging operation on the momentum equations as in Eqs. (1) and (2), we throw away all details concerning the state of flow contained in the instantaneous fluctuations.

As a result six additional unknowns are obtained: the Reynold stresses $\rho\overline{u_i' u_j'}$. These turbulent stresses are usually very large compared to the viscous stresses in a turbulent flow and influence the fluid behaviour substantially. It is the main task of turbulence modelling to predict the Reynold stresses in order to close the equations in an appropriate way.

The simplest "complete" models of turbulence are two equation models in which the solution of two separate transport equations allows the turbulent velocity and length scales to be determined independently. In the CFD community they are known as the k–ε models [34,35]. The k–ε models are based on transport equations for the turbulence kinetic energy k and its dissipation rate ε.

One of them, the realizable k–ε model, satisfies certain mathematical constraints on the Reynolds stresses consistent with the underlying physics of turbulent flows [36]. Experimental and theoretical studies have shown that the realizable k–ε model provides the best performance of all k–ε model versions for a wide range of flows with complex secondary flow structures [36,37].

The closure transport equations for the realizable k–ε model are:

$$\frac{\partial}{\partial t}(\rho k)+\frac{\partial}{\partial x_i}(\rho k u_i)=\frac{\partial}{\partial x_j}\left[\left(\mu+\frac{\mu_t}{\sigma_k}\right)\frac{\partial k}{\partial x_j}\right]+G_k+G_b-\rho\varepsilon-Y_M \tag{3}$$

$$\frac{\partial}{\partial t}(\rho\varepsilon)+\frac{\partial}{\partial x_i}(\rho\varepsilon u_i)=\frac{\partial}{\partial x_j}\left[\left(\mu+\frac{\mu_t}{\sigma_\varepsilon}\right)\frac{\partial\varepsilon}{\partial x_j}\right]+\rho C_1 S\varepsilon \tag{4}$$

$$-\rho C_2\frac{\varepsilon^2}{k+\sqrt{v\varepsilon}}+C_{1\varepsilon}\frac{\varepsilon}{k}C_{3\varepsilon}G_b$$

In these equations, G_k represents the generation of turbulence kinetic energy due to the mean velocity gradients, G_b is the generation of turbulence kinetic energy due to buoyancy, Y_M represents the contribution of the fluctuating dilatation in compressible turbulence to the overall dissipation rate. μ denotes the Newtonian viscosity, μ_t the turbulent viscosity and v is the kinematic viscosity, and σ_k and σ_ε are the turbulent Prandtl numbers for k and ε respectively. C_2 and $C_{1\varepsilon}$ are coefficients that assure realizability and are of major importance. Realizability is defined as the requirement of the non-negativity of turbulent normal stresses and the Schwarz' inequality between any fluctuating quantities ($\overline{u_i u_j}^2 \le u_i^2 u_j^2$). As one can see, realizability is in fact the minimal requirement to prevent a turbulence model from producing non-physical results [38].

3.2. Equation of motion for the particles

The trajectories of the nanoparticles are predicted by integrating their equations of motion in a Lagrangian reference frame. These equations are in fact force balances that equate the particle inertia with the forces acting on the particle. Along their trajectories the particles can exchange momentum, mass, and energy with the fluid phase. The dispersion of the particles due to turbulence in the fluid was calculated using a stochastic tracking model [39]. This random walk model includes the effect of instantaneous turbulent velocity fluctuations on the particle trajectories. By computing the trajectory in this manner for a sufficient number of representative particles, the random effects of turbulence were accounted for. Coagulation due to electrostatic forces was considered to be negligible. Apart from that, particle accretion at wall boundaries was neglected, as was experimentally verified recently [40]. Instead elastic collisions with the walls of the ablation setup were assumed to occur.

The equation for particle motion in a Lagrangian reference frame is given as:

$$\frac{d\vec{u}_p}{dt}=\vec{F}_{drag}+\vec{F}_{gravitation}+\vec{F}_{pressure}+\vec{F}_{lift}+\vec{F}_{vm} \tag{5}$$

$\vec{F}_{drag}$ is the drag force per unit mass, $\vec{F}_{gravitation}$ is the gravitation force, $\vec{F}_{pressure}$ is a force due to the pressure gradient in the fluid, $\vec{F}_{lift}$ is the lift force and $\vec{F}_{vm}$ is the virtual mass force.

3.2.1. Drag force

Drag is made up of friction forces, which act in a direction parallel to the surface of a particle.

For a drag force acting on a sphere, several expressions are used in the literature [41,42]. The expression for the drag, which includes the Cunningham correction to the Stokes drag force per unit mass, is given by [41]:

$$\vec{F}_{drag}=\frac{3\mu}{4\rho_p d_p^2}\frac{C_D Re_p}{C_C}\left(\vec{u}-\vec{u_p}\right) \tag{6}$$

where $\vec{u}$ is the fluid velocity vector, d_p is the particle diameter, μ is the coefficient of viscosity, C_c is the Cunningham correction factor given by [41]:

$$C_c=1+\frac{2\lambda}{d_p}\left[1.257+0.4\ \exp\left(-1.1\left(d_p/2\lambda\right)\right)\right] \tag{7}$$

and Re_p, the relative particle Reynolds number, is defined as

$$Re_p=\frac{\rho\left(\vec{u}-\vec{u_p}\right)d_p}{\mu} \tag{8}$$

As can been seen from Eq. (7), the Cunningham correction factor is particularly important for sub-micron particles, since the particle radius becomes comparable with the fluid mean path λ.

In that case the assumption of zero gas velocity at the particle surface is no longer valid (*slipping effect*).

The drag coefficient C_D, which accounts for the Reynolds number correction to the Stokes drag, is given as [41]:

$$C_D=\frac{24}{Re_p}\left(1+0.15Re_p^{0.687}\right) \tag{9}$$

The non-linear corrections are expected to be significant only for larger particles with appreciable slip velocity. For nanoparticles with small slip velocity, *Re* is very small and the second term in Eq. (9) will be negligible.

3.2.2. Gravitation force

The force due to gravitation is given by:

$$\vec{F}_{gravitation}=\frac{\vec{g}(\rho_p-\rho)}{\rho_p}$$

where $\vec{g}$ denotes the gravitational acceleration and ρ_p is the particle mass density.

3.2.3. Pressure force

An additional force arises due to the pressure gradient in the fluid, that controls the forward motion of the particles:

$$\vec{F}_{pressure}=-\frac{\rho}{\rho_p}u_{p,i}\frac{\partial u}{\partial x_i}(i=1,2,3) \tag{10}$$

where $u_{p,i}$ are the particle velocity components and ρ_p is the particle mass density.

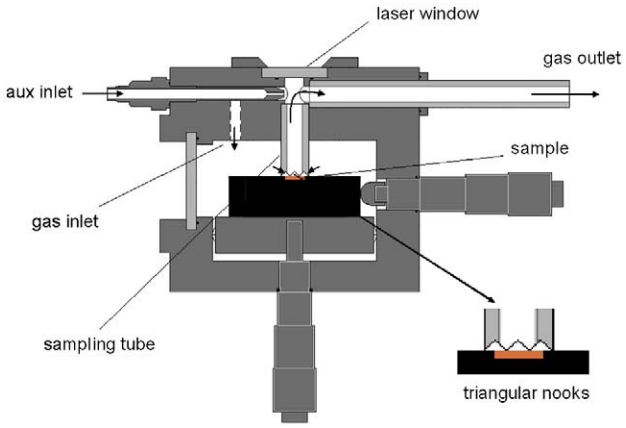

Fig. 1. The ablation cell used. Laser sampling is performed into a glass sampling tube in the middle of the cell which is in contact with the sample surface. The transport gas flows into the sampling tube through four triangular nooks, as shown in the detailed picture.

3.2.4. Lift force

Finally the lift force was considered. Small particles in a shear field experience a lift force perpendicular to the direction of flow. The shear lift originates from the inertia effects in the viscous flow around the particle and is fundamentally different from the aerodynamic lift force. The actual applied lift force is a generalization of the relation provided by Saffman for three-dimensional shear fields [43–45]. The expression for the Saffman lift force is restricted to small particle Reynolds numbers. In addition, the particle Reynolds number based on the particle–fluid velocity difference must be also smaller than the square root of the particle Reynolds number based on the shear field.

3.2.5. Other forces

As was shown by Ounis and Ahmadi [46], other hydrodynamical forces such as the Basset force, the Faxen correction, are much smaller than the Stokes drag force for small particles. Therefore, they were neglected in Eq. (5). At the end, the virtual mass force required to accelerate the fluid surrounding the particle was included. Since this force becomes significant when the particle density is smaller then the fluid phase density, it was of less importance.

4. Computational conditions

4.1. Experimental setup

Experimentally two types of ablation measurements have been run: particle size distribution measurements and measurements of the transient signals occurring in fs-LA-ICP-MS using a sampling tube cell.

The setup for the particle distribution measurements can be found in [47,48], whereas the data used in the present paper are taken from [49]. Therefore, the setup is only shortly presented here. A brass sample (Cu 60.6%, Zn 39.4%) was placed in an ablation cell and material was removed from it using a fs-laser (Hurricane, Spectra Physics, $\lambda = 795$ nm, pulse length: ~120 fs). On the sample surface the diameter of the Gaussian beam accounted for 70 μm and the peak-fluence applied was 1.7 J/cm^2. Each of 15 craters was ablated for 32 s at a repetition rate of 10 Hz. The removed material was transported by a 1 L/min helium flow into a low-pressure impactor (ELPI, Dekati). There the aerosol was sorted by size and collected concurrently. Subsequently the material was dissolved and the aerosol mass was measured by total reflection X-ray fluorescence (TXRF).

For the dispersion measurements a sampling tube ablation cell has been used (Fig. 1). It has already been employed in [25]. The inner diameter of the sampling tube was 5.5 mm. The auxiliary inlet of the chamber has been sealed for the present measurements. The brass sample was ablated using the above mentioned fs-laser. The laser beam had a fluence of 6.5 J/cm^2 at the sample surface while the beam diameter was 65 μm. Single shots were applied. The ablated material was transported from the cell via a 40 cm long tygon tube (inner diameter: 4 mm) into the ICP (HP4500, Agilent). Helium or argon were used as transport gases. Additional argon was added via a Y-connector

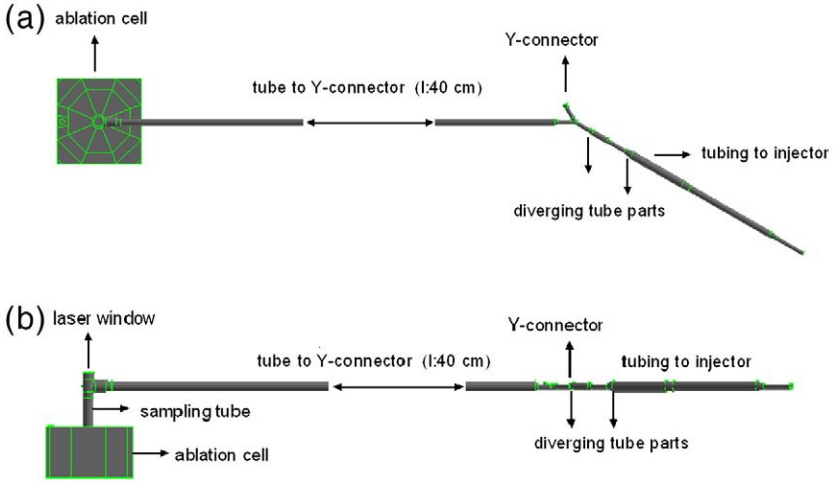

Fig. 2. Top view (a) and side view (b) of the simulated ablation setup.

just before the ICP-torch. In the Ar/Ar case (cell gas: Ar) a flow rate of 0.83 L/min argon flowed through the cell and 0.79 L/min argon was added. In the He/Ar case 1.3 L/min helium passed through the cell and 1.55 L/min argon was added. The ICP was operated at 1.35 kW. Data points were taken every 10.5 ms. The ^{67}Zn and the ^{65}Cu isotopes were measured, setting the integration time per data point to 4 ms and 2 ms, respectively.

4.2. Meshed design

The ablation setup to be simulated (see Fig. 2) was built on scale and divided into 300 000 control volumes. The mesh was constructed by means of regular, hexahedral elements and boundary layers. Boundary layers are used primarily to control mesh density and, thereby, to control the amount of information available from the computational model in specific regions of interest. In this case the boundary layers were attached at the gas inlets/outlets and the wall of the ablation setup. Subsequently, the grid was refined systematically until the solution of the flow equations was found to be independent of the grid size. This condition was reached for a grid that consisted of 400 000 cells. The high quality mesh resulted in a very fast convergence: within 3 h the steady state flow pattern was calculated. Details of the outer box and sample tube are shown in Fig. 3.

4.3. Boundary conditions and physical properties

Tables 1 and 2 summarize the different gas parameter settings that were used in the calculations. Compared to [23,24,26] the Hagen–Poiseuille law was not used, since it can only be applied for laminar flows in pipes with circular cross-sections. For that reason the actual inlet flow rates were applied. The carrier and auxiliary gases were treated as compressible ideal gases. The Newtonian viscosity, heat capacity and thermal conductivity of the different gases were obtained using kinetic theory [50,51].The well known

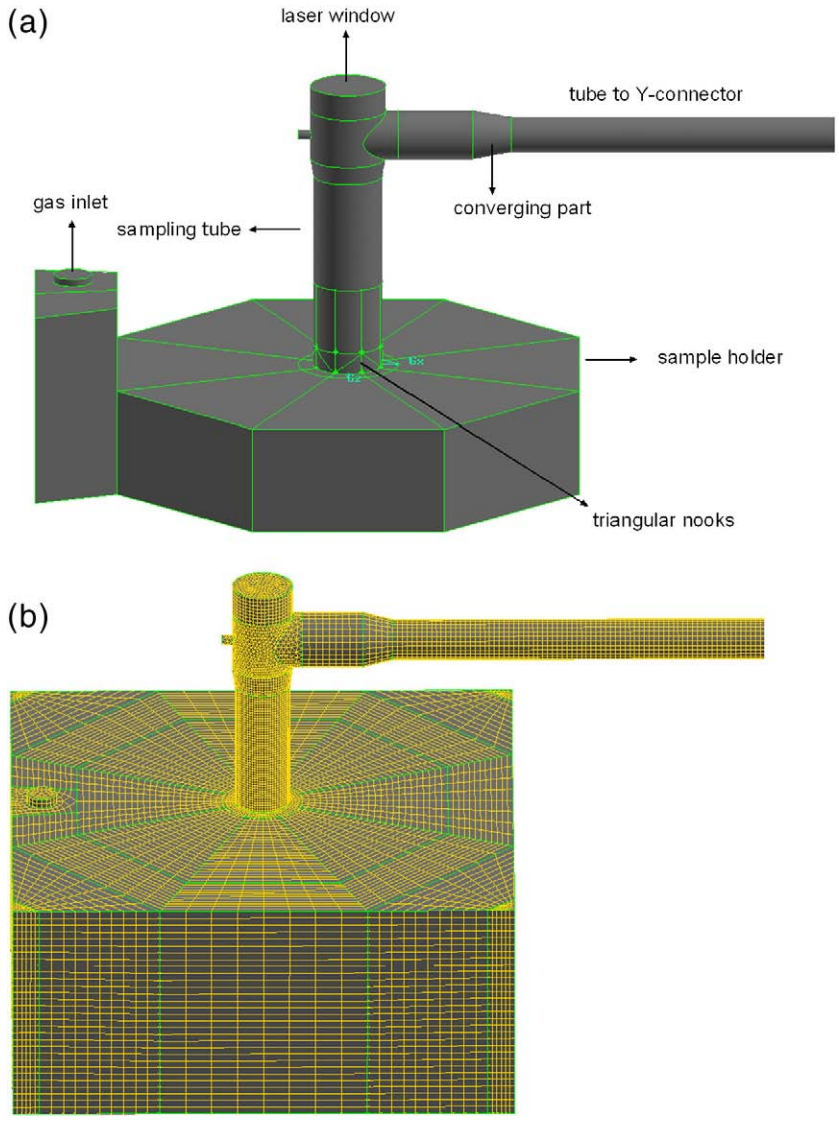

Fig. 3. (a) Details of the ablation chamber. (b) Detail of the hexahedral mesh of the outer box and sampling tube.

Table 1
Flow gas parameters used in simulations

Parameter	Value	Parameter	Value
Gas type in outer chamber	Ar/He	Flow rate in outer chamber (l/min)	0.79/1.3
Gas type in Y-connector	Ar	Flow rate in Y-connector (l/min)	1.55
Mass Ar (amu)	39,9480	Mass He (amu)	4,0026
Temperature (K)	300	outlet (Pa)	101325

Lennard–Jones potential was applied to calculate the viscosity and thermal conductivity [51]. This potential was defined by means of two parameters: the collision diameter σ and the characteristic energy ε (given in Table 2).

4.4. Particle size distribution

The experimentally measured particle size distribution is shown in Fig. 4. In this graph the masses of Cu and Zn have been added for each size range. Most of the mass can be found in a size range of particles smaller than about 50 nm but there is also an important amount of mass to be found in medium sized particles (around 250 nm diameter). The mean value for the ablated mass per shot accounted for 0.65 ng, using a fluence of 1.7 J/cm^2.

The *measured* particle size distribution was inserted in the computational model, using the Rosin–Rammler relation [52]. The complete range of sizes was divided into an adequate number of intervals; each represented by a mean diameter for which trajectory calculations were performed.

As a result, the experimentally measured size distributions of Zn and Cu were divided in 3 main classes: small particles, medium sized particles and big particles. Every class was further divided in channels that corresponded to a certain particle size. Since the particle size distribution produced under short-pulse irradiation is shifted towards the smallest particles, a high size resolution was necessary in that region. Therefore the class of the smallest particles was further divided in 50 channels, meanwhile the classes of the medium and big sized particles were each divided in 25 channels.

The particles were ejected from the crater surface (d=70 μm) in the sampling tube at a velocity of 500 m/s. This initial velocity was estimated by applying momentum conservation on the plasma plume velocity. The calculation of the plasma plume velocity was based on the models described in refs. [53,54].

Finally the original size distribution was modified. Additional particles were added to the tails of the size distribution in order to mimic the *ablated* size distribution. In both cases, the 150 channels were simulated for 36 h and 100 000 individual particle trajectories were tracked.

Table 2
Lennard–Jones potential parameters used in the kinetic treatment of the physical properties

Parameters of the Lennard–Jones potential	σ (A°)	ε/k_b (K)
Ar	3.542	93.3
He	20.95	10.22

5. Results and discussion

The computations were conducted for pure argon and helium–argon mixtures. The inlet conditions were kept constant in both cases. In the next section we will omit the graphical representation of the pure argon flow patterns, since they are qualitatively similar compared to the mixture case.

5.1. Flow pattern and turbulent zones

The gas flow pattern in the ablation cell is represented for the mixture case (He/Ar) in Fig. 5. Note that for sake of clarity only a few of the hundreds of flow lines are presented, for sake of clarity.

As can been seen from this figure, the flow lines in the outer chamber consist of some vortices next to the flow inlet. The onset for the flow is turbulent, but the flow pattern in the sample tube is clearly laminar. Indeed, the small triangular nooks at the side of the sample (see Fig. 1), guarantee a reproducible, well separated, laminar flow pattern in the sampling tube [25]. Furthermore a weak turbulent zone is observed in the volume under the laser window (see detail in Fig. 5). Due to the slight pressure difference and the converging tube part at the exit of the central tube (see Fig. 3), the laminar flow pattern is, however, nicely conserved till it reaches the Y-connector. Similar observations were made in [25,26].

At the Y-connector, however, the situation changes considerably (see Fig. 6). The flow of the auxiliary flow gas, Ar, pushes the carrier gases (He or Ar) that arrive from the sample chamber towards the wall. As a result surface friction is induced that causes the formation of small eddies in the wall region opposite to the argon gas inlet (Fig. 6a.). Moreover, a considerable amount of kinetic energy is dissipated in the boundary layer, slowing down the He/Ar-gas next to the boundary.

At the diverging parts of the tubing connecting the Y-connector and the injector, a clearly turbulent flow pattern is found. Note that this was also observed in [26]. The influence of

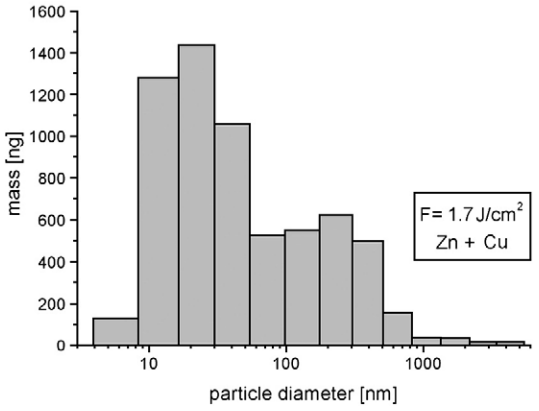

Fig. 4. The experimentally measured size distribution of brass for a laser fluence of 1.7 J/cm^2.

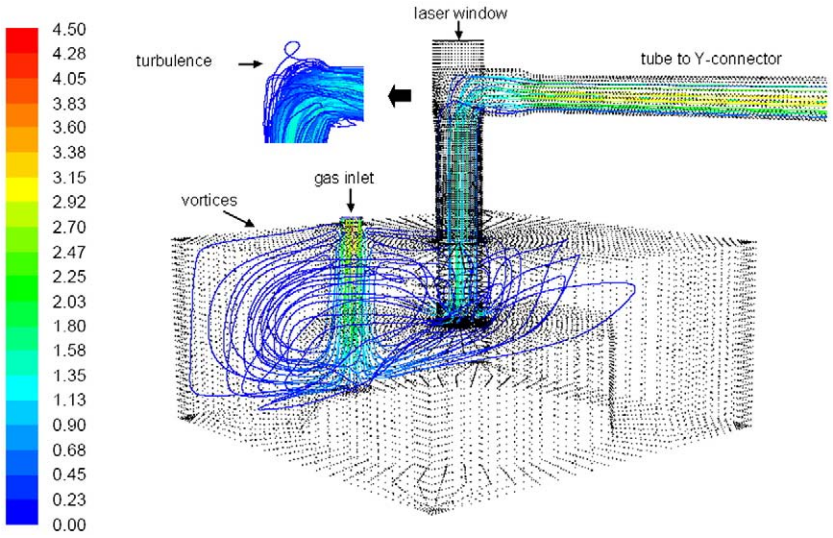

Fig. 5. The calculated flow pathlines for the mixture case (He/Ar) are shown in terms of velocity (m/s) for the outer chamber and the sampling tube. For the sake of clarity, 80% of the carrier gas pathlines were omitted. At the inlet of the outer chamber rotational flow structures are observed. The flow in the sampling tube and transport tube is, however, clearly laminar, except in the zone under the laser window. A detail of the full flow pattern nearby the laser window is shown.

these turbulent regions on the particle transport is far more important than the one nearby the laser window (see below).

In Fig. 6b. the turbulent intensity is depicted:

$$I_{\text{turb}} = \frac{u'_{\text{rms}}}{U_{\text{mean}}} \tag{11}$$

with

$$u'_{\text{rms}} = \sqrt{\tfrac{1}{3}\left(u_x'^2 + u_y'^2 + u_z'^2\right)}, U = \sqrt{U_x^2 + U_y^2 + U_z^2}$$

In Eq. (11) u'_{rms} is the root-mean-square of the turbulent velocity fluctuations and U the mean velocity. From Fig. 6b. one can clearly see that the turbulence level in the wall layer opposite to the Y-connector is twice as high as the ones found in the other regions of the tube.

5.2. Particle trajectories

As stated in the beginning of the previous section, the flow behaviour for the mixture case and pure argon case were qualitatively the same. From a quantitative point of view, however, this was not the case at all. In the mixture case a maximum velocity of 21.5 m/s was found, whereas the argon case had a maximum value of 8.5 m/s. These observations are a

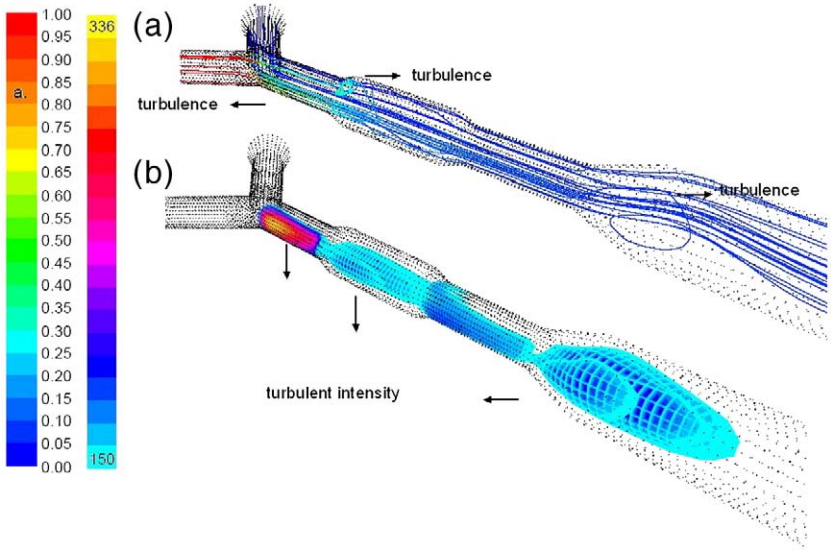

Fig. 6. In (a) The flow pattern for the mixture case (He/Ar) in the tubing connecting the Y-connector and injector is shown in terms of the mass fraction of He (red is 100% He, blue lines correspond to 0% He or 100% Ar). For sake of clarity, a part of the pathlines were omitted. In part (a) the three turbulent regions are shown. At the diverging tube parts one can clearly observe the eddies. In (b) the zones of maximum turbulent intensity (%) are represented. The turbulent intensity represents the ratio of the turbulent velocity fluctuations and the mean flow velocity. The wall layer opposite the Y-connector has a much higher turbulent intensity compared to the other regions, although this was not clearly visible in (a).

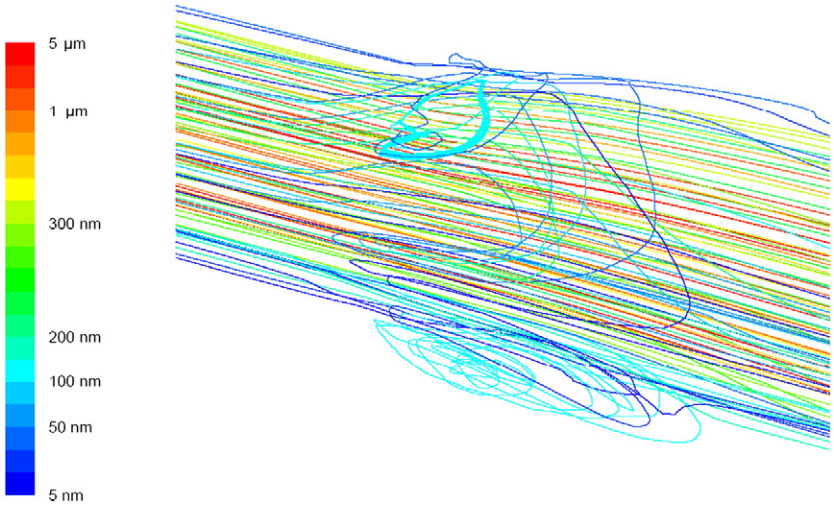

Fig. 7. The calculated flow pattern of the particles for the mixture case (He/Ar) in the tubing connecting the Y-connector and injector is shown in terms of the particle sizes. The different particles sizes were tracked as a function of time and their trajectories were calculated. It is clearly observed that he smaller particles could escape less efficient out of the turbulent region.

direct consequence of the mass difference of both gases. Furthermore the turbulent intensity in the mixture case went up to 300%, whereas the turbulent intensity for the pure argon case was only 150%. These results can mainly be attributed to the difference in velocity of both gas types. Due to the difference in inertia of argon and helium and the increased diffusivity compared to the pure argon case, the surface friction induced by argon at the wall opposite to the Y-connector is much higher in the mixture case. As a consequence the transit times of the particles through the tubing and signal behaviour were substantially different for the two cases.

Since the laser induced particles are confined in the flow gas coming from the sampling tube, their trajectories are clearly affected by the turbulent regions. In order to retrieve the particles that did not leave the injector side, different circular cross-sections were defined along the tubing. When the particles did not flow through the cross-sections it meant that they settled down in the tubing and the calculation of the trajectory was aborted. From these calculations it was observed that the turbulent flow behaviour at the Y-connector and in the diverging tube parts appeared to promote the entrapment of the smallest particles (diameter < 200 nm).

The particles in the range 5 nm–5 µm reveal some interesting physical phenomena as soon as they arrive in the turbulent tube parts. Both in the mixture case and the pure argon case it was observed that a fraction of the smaller particles in the range (1 nm–200 nm) was trapped by the eddies (see Fig. 7.). In the case of pure argon, however, the size-dependent separation in the turbulent regions was much weaker. In both cases the particles with sizes 300 nm–5 µm followed the path lines between the eddies. These results can be explained as follows: Due to their inertia the bigger particles escape the turbulent zones more effectively than the smaller particles. Since the turbulent regions are weaker in the case of pure argon, the size-separation of the particles due to turbulence is smaller.

Finally the transit times of the particles were calculated (see below). It was found that the particles were transported more efficiently in the mixture case. This result is a direct consequence of the higher velocity of the mixed gas flow compared to the pure argon flow. Moreover it was seen that the bigger particles had shorter transit times then the smaller ones. As a result a second type of size-separation occurred. Due to the drag force, bigger particles were transported faster than smaller ones. By keeping the viscosity and relative particle velocity constant in Eq. (6) we can obtain the "drag ratio" d/C_c. The drag ratio illustrates the evolution of the drag force in terms of the particle diameter (see Fig. 8.). Since the mean free path of He (200 nm) is four times as high as the mean free path of Ar (70 nm), the drag force in the mixture case will be smaller and slipping effects are more pronounced (see Eq. (7)). As a result, Ar provides a more effective transport of particles in the whole

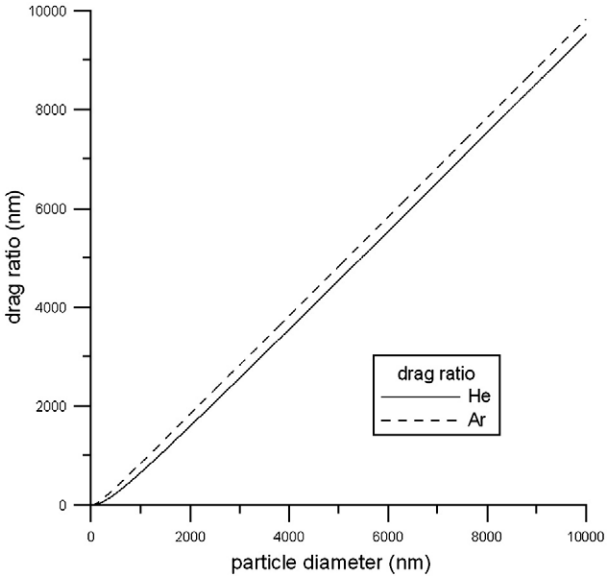

Fig. 8. The drag ratio is shown for Ar and He in terms of the particle sizes. It is clearly observed that Ar provides more efficient particle transport in the whole size range.

Table 3
Calculated mass extraction efficiency and mass losses in the different parts of the setup, for pure Ar and the He/Ar mixture

Flow gas	Mass extraction efficiency (%)	Mass loss (%): total setup	Ablation cell	Tubing zone A	Tubing zone B
He/Ar mixture	93	7	2	0	5
Ar	95	5	3	0	2

Tubing zone A denotes the tube between the ablation cell and the Y-connector, tubing zone B denotes the tubing towards the injector and includes the Y-connector.

size range, provided that the relative particle velocity and viscosity of both gases are the same.

The findings described in this section are consistent with the observations made in [23,24,27].

5.3. Mass extraction efficiency

In order to obtain the mass extraction efficiency, the masses of the particles that reached the injector side (i.e., the entrance to the ICP) were summed. Knowing the original ablated single shot mass and the escaped total mass, the mass extraction efficiency could be calculated. In order to check the consistency of the model, the experimentally measured size distribution of the particles was inserted and 100% mass extraction efficiency was found. Afterwards the adapted particle size distribution (see par. 4.) was inserted. The results for pure Ar and the He/Ar mixture are summarized in Table 3.

The observed similar mass extraction efficiencies for the mixture case and the pure argon case are consistent with the experimental findings. Indeed, typical values for the mass extraction efficiency of 80% (uncertainty +20%–10%) and 90% (±10%) of fs-LA-ICP-MS under similar flow conditions were reported for both He/Ar and pure Ar [25,55].

The similar mass extraction efficiencies are a direct consequence of the effects described above.

In the sampling tube the drag force and gravity force are opposed. As a result, the big particles (diameter > 5 μm) are less efficiently transported by argon due to the lower gas velocity and gravity tends to settle them down in the sampling tube. In contrast, the vortices in the tube connecting the Y-connector and injector trap the small particles in the mixture case and tend to deposit them at the walls. These effects are the reason for the slight differences in mass losses in the ablation cell and tubing zone B.

5.4. Signal reconstruction

It is clear from the observations made in Section 5.2 above that the combined action of the gas velocity and turbulence determines the time spread of the particles. In the present design, higher gas velocities will reduce the washout-time and improve the signal, but will also cause more turbulence in the tube connecting the Y-connector and injector to the ICP. Since turbulence acts as a barrier on ultra-fine sized particles, it can cause significant broadening and splitting of the fs-LA-ICP-MS signals.

In order to obtain a deeper understanding of the influence of both effects in the mixture case and the pure argon case, a signal was constructed based on the wash-out times of the particles.

In both cases a bimodal pattern was observed. The calculated total signal for the brass particles in the He/Ar case (see Fig. 9.) consists of two peaks: the first peak has a maximum at 0.18 s, whereas the second peak shows a maximum at 0.21 s. All the particles in the size range (300 nm–5 μm) were contained in the first peak. Moreover 88% of the particles in the size range (1 nm–200 nm) were found in the second peak. Hence, this shows that the biggest particles are characterized by the shortest transit times, whereas both smaller and mean sized particles have in general longer transit times. Since the smaller particles escape less efficiently from the turbulent regions, most of them are contained in the second peak. The modelled signal in Ar consisted also of two main peaks. The first one started at 0.58 s and ended at 0.68 s, the second started at 0.75 s and ended at 0.95 s. The signals were much broader compared to the signal in He/Ar (see Fig. 10.) and the maximum peak height was 1.5 times as low compared to the mixture case. These observations are a direct consequence of the lower gas velocity of argon. Since the size-separation due to turbulence and slipping effects was smaller in the case of pure argon, a separate left peak including the big sizes as found in the mixture case was not observed. Because the turbulent effects were smaller, the second signal peak was far more shifted to the right compared to the mixture case. Besides, additional fine structure was found in the second main peak. Indeed, two small peaks are observed at 0.8 s and 0.87 s. In fact one could consider the peak pattern in the argon case as “trimodal”. This is attributed to the interplay of turbulence and velocity. Since the particles in the argon case move slower compared to the mixture case, the lags in time caused by the entrapment in the vortices are clearly observed.

In order to check our model calculations, we have compared these theoretical ICP–MS signals with experimental signals

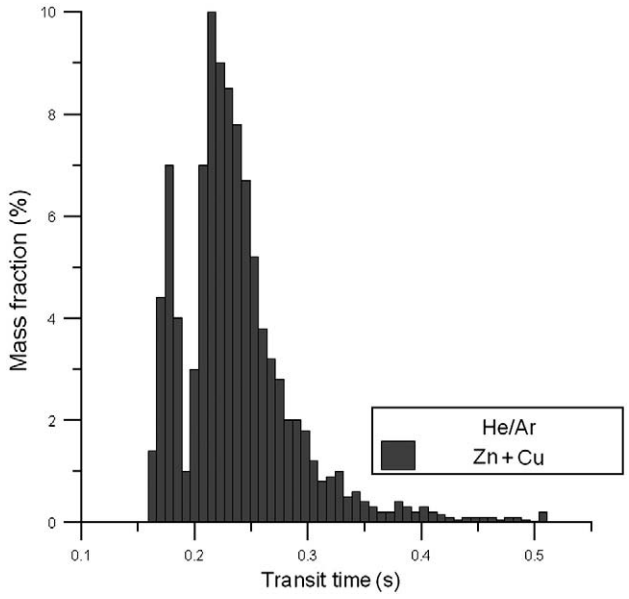

Fig. 9. Modelled bimodal brass signal for He/Ar.

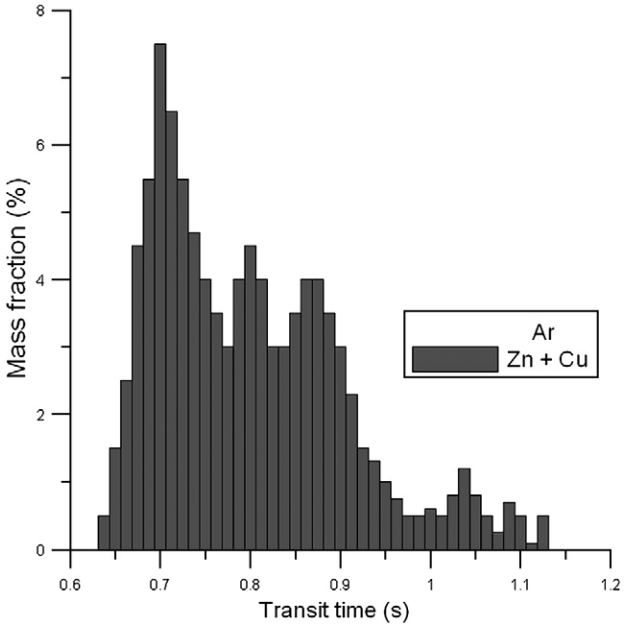

Fig. 10. Modelled trimodal brass signal for Ar.

from [25,56]. The latter are shown in Fig. 11. and Fig. 12. for the He/Ar case and the pure Ar case, respectively. The represented signals are each an average of five measurements of single shots applied onto the same spot of the sample.

The calculated brass signal in He/Ar as shown in Fig. 9 and the measured signal in Fig. 11. are clearly similar. Both signals have a peak width of 0.15 s and the relative peak heights of the modelled signal (10/7) and the measured signal (10/8) match nicely.

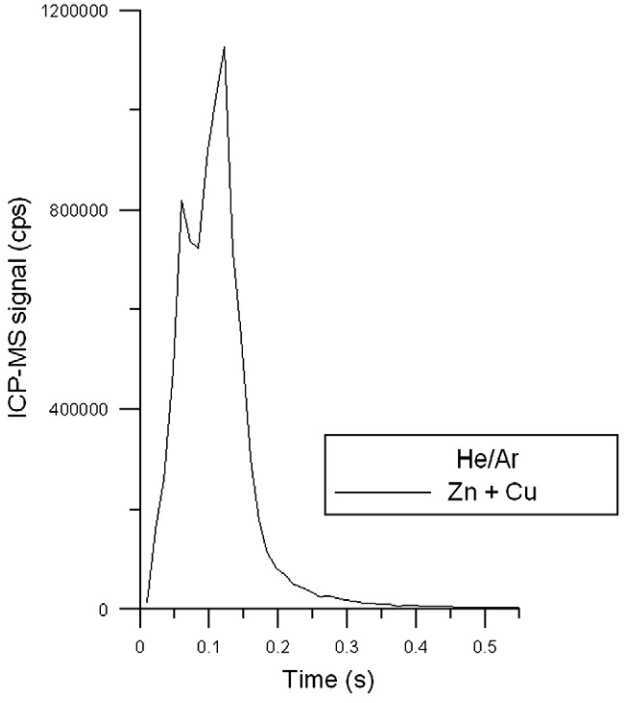

Fig. 11. Measured $^{67}Zn+^{65}Cu$-ICP-MS signal for the He/Ar case.

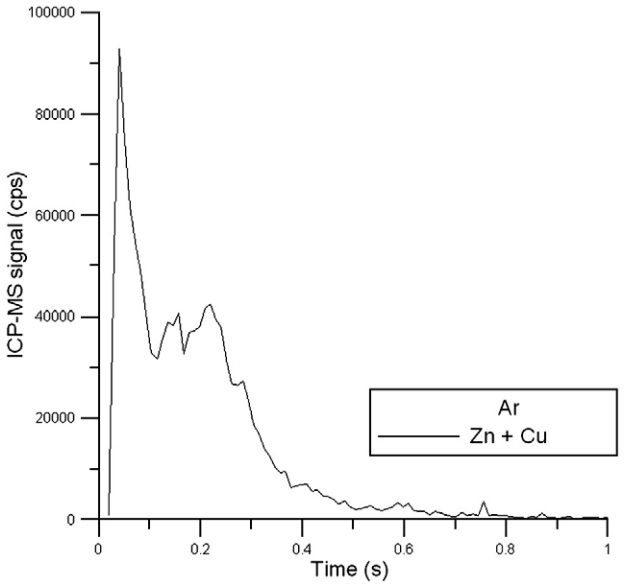

Fig. 12. Measured $^{67}Zn+^{65}Cu$-ICP-MS signal.

In the case of argon both signals reveal two main peaks characterized by an increase in signal width and a clear reduction in signal intensity, compared to the mixture case. Besides it is clearly observed that the second peak is much lower than the first peak and exhibits some additional fine structure. Similar observations were made in ref. [26,27].

5.5. Design optimization

The structure in the (calculated and measured) signal leads to an undesired elongation of the wash-out time compared to the expected one without structuring. Although the cell investigated in this study has already a relatively short wash-out time compared to other cells (see [25]) it would be nice if the wash-out time could be reduced further. An assembly with short wash-out times is beneficial when measurements are performed that need the separation of many single shots. Such measurements can be, for instance, 2D surface-mapping or depth-profile measurements. Indeed, short wash-out times can diminish errors due to material still present from earlier shots and/or the measurement time can be reduced significantly. Furthermore, as the same amount of material is transported one could obtain a higher signal compared to longer wash-out times. So, higher S/N-ratios could be achievable — assuming the likely case that the noise stays the same.

From the discussion above it becomes clear that the turbulent effects should be minimized in order to obtain a reduced width of the fs-LA-ICP-MS signals and to increase the signal-to-noise ratio. As demonstrated in the previous sections, the Y-connector and diverging tubing parts appear to be responsible for the signal deterioration.

In 2004, Halicz and Günther reported similar findings [57]. In order to reduce the resonance in the tubing, they came up with a new design optimization. They removed the Y-connector and applied a coaxial bulb mixer that was adapted from [17]. The bulb was used as a mixing tool between the two gas flows.

Helium was added at 90° to the argon flow and mixed after the perpendicular introduction. Then the adapter was conically reduced in diameter. The device was expected to maintain a laminar gas flow compared to the use of T- and Y-connectors. Moreover it was expected to be less affected by the pressure differences between the two carrier gases.

In 2006 Pisonero et al. [58] developed a novel ablation cell for LA-ICP-MS. The so called high efficiency aerosol dispersion (HEAD) ablation cell was based on the use of a directed gas flow expansion of the aerosol and a ventury effect created by two nozzles to extract aerosol into the main make up gas stream. The HEAD cell was able to modify the laser generated aerosol, by shifting the original particle size distribution towards smaller particle sizes. For both cells it was observed that the stability and reproducibility of the ion-signals improved significantly.

In the near future we will develop new design optimizations based on the observations described above (see Section 5.4) and reported by [57,58]. In all cases the Y-connector and diverging tube parts will be removed and designs will be developed that sustain laminar flow, exhibit reduced temporal dispersion, allow quasi loss — less particle transport and guarantee reproducible analytical signals under a wide range of flow conditions.

6. Conclusion

Computational fluid dynamics was used to analyze the transport of near infrared femtosecond (fs) laser generated brass aerosols during sample introduction for ICP-MS analysis. A detailed computational strategy was developed in order to mimic the experiment as good as possible.

The modelled ablation setup including the sample chamber, sample holder, Y-connector and diverging–converging tubing towards the injector was modelled at once. The mass transport efficiency and transit times of the brass aerosols in pure argon and helium–argon mixtures were calculated at optimized conditions. Based on the wash-out times of the aerosol particles, transient signals were constructed for both cases. Finally the modelled results were compared with experimental data.

The modelled and experimental results revealed that the calculated mass transport efficiency (~90%) was independent of the carrier gases. Besides, the modelled transient signals were in excellent agreement with the experimentally recorded ICP-MS signals.

In both cases bimodal (or even trimodal) signals were observed, that were found to originate from turbulent effects in the tube connecting the Y-connector and the injector. Since the structure in the calculated and measured signals leads to an undesired elongation of the wash-out times, new design optimizations are desirable. Similar observations were made in refs. [17,57,58]. Accordingly new design optimizations will be suggested in the near future based on the modelled results and the findings of refs. [17,57,58].

In general this paper illustrates that CFD simulations are able to present a realistic and detailed picture of the gas flow and particle transport. Hence, they can be used to assist in the development and optimization of ablation setups.

Acknowledgements

Funding by the Flemish Fund for Scientific Research (FWO Vlaanderen) and by the Deutsche Forschungsgemeinschaft (DFG) are gratefully acknowledged. Other financial support comes from the Federal Services for Scientific, Technical and Cultural Affairs (DWTC/SSTC) of the Prime Minister's Office through IUAP-VI. We thank the excellent calculation support of the core facility CALCUA, provided by the University of Antwerp. The authors also thank the Ministry of Innovation, Science, Research, and Technology of the state Northrhine-Westphalia and the Ministry of Education and Research of the Federal Republic of Germany for the general support.

References

[1] A. Vertes, R. Gijbels, F. Adams, Laser Ionization Mass Analysis, Wiley VCH, 1993.
[2] J.A.C. Broekaert, Analytical Atomic Spectrometry with flames and plasmas, Wiley VCH, 2002.
[3] B. Fairman, M. Hinds, S.M. Nelms, D.M. Penny, P. Goodall, Industrial analysis: metals, chemicals and advanced materials, J. Anal. At. Spectrom. 15 (2000) 1606–1631.
[4] I. De Raedt, K. Janssens, J. Veeckman, L. Vincze, B. Vekemans, T.E. Jeffries, Trace analysis for distinguishing between Venetian and façon-de-Venise glass vessels of the 16th and 17th century, J. Anal. At. Spectrom. 16 (2001) 1012–1017.
[5] J.S. Becker, Applications of inductively coupled plasma mass spectrometry and laser ablation inductively coupled plasma mass spectrometry in materials science, Spectrochim. Acta Part B 57 (2002) 1805–1820.
[6] D. Günther, Laser ablation-inductively coupled plasma mass spectrometry trends, Anal. Bioanal. Chem. 372 (2002) 31–32.
[7] D. Bleiner, P. Lienemann, A. Urich, H. Vonmont, A. Wichser, Spatially resolved quantitative profiling of compositionally graded perskovite layers using laser ablation-inductively coupled plasma mass spectrometry, J. Anal. At. Spectrom. 18 (2003) 1146–1153.
[8] C.A. Heinrich, T. Pettke, W.E. Halter, M. Aigner-Torres, A. Audétat, D. Güenther, B. Hattendorf, D. Bleiner, M. Guillong, I. Horn, Quantitative multi-element analysis of minerals, fluid and melt inclusions by laser-ablation inductively-coupled-plasma mass-spectrometry, Geochim. Cosmochim. Acta 67 (2003) 3473–3497.
[9] S.D. Müller, R.A. Diaz-Bone, J. Felix, W. Goedecke, Detection of specific proteins by laser ablation inductively coupled plasma mass spectrometry (LA-ICP-MS) using gold cluster labelled antibodies, J. Anal. At. Spectrom. 20 (2005) 907–911.
[10] S.F. Durrant, N.I. Ward, Recent biological and environmental applications of laser ablation inductively coupled plasma mass spectrometry (LA-ICP-MS), J. Anal. At. Spectrom. 20 (2005) 821–829.
[11] Q. Bian, C.C. Garcia, J. Koch, K. Niemax, Non-matrix matched calibration of major and minor concentrations of Zn and Cu in brass, aluminium and silicate glass using NIR femtosecond laser ablation inductively coupled plasma mass spectrometry, J. Anal. At. Spectrom. 21 (2006) 187–191.
[12] A. Gray, Solid sample introduction by laser ablation for inductively coupled plasma source mass spectrometry, Analyst 5 (1985) 551–556.
[13] L. Moenke-Blankenburg, Laser-inductively coupled plasma spectrometry, Spectrochim. Acta Rev. 15 (1993) 1–37.
[14] L. Moenke-Blankenburg, M. Gaeckle, D. Güenther, J. Kammel, in: K.E. Jarvis, A.L. Gray (Eds.), Plasma Source Mass Spectrometry, Royal Society of Chemistry, Cambridge, UK, 1989.
[15] J. Růžíka, E.H. Hansen, Flow injection analysis Wiley–Interscience, 1988.
[16] A.M. Leach, G.M. Hieftje, Factors affecting the production of fast transient signals in single shot laser ablation inductively coupled plasma mass spectrometry, Appl. Spectrosc. 56 (2002) 62–69.
[17] D. Bleiner, D. Günther, Theoretical description and experimental observation of aerosol transport processes in laser ablation inductively

coupled plasma mass spectrometry, J. Anal. At. Spectrom. 16 (2001) 449–456.
[18] D. Bleiner, PhD Dissertation nr 14665, ETH Zürich, 2002.
[19] A. Plotnikov, C. Vogt, K. Wetzig, An approach to the reconstruction of true concentration profile from transient signal in spatially resolved analysis by means of laser ablation ICP MS, J. Anal. At. Spectrom. 17 (2002) 1–8.
[20] M. Gäckle, D. Merten, Modelling the temporal intensity distribution for laser ablation-inductively coupled plasma mass spectrometry in single shot mode, Spectrochim. Acta Part B 59 (2004) 1893–1905.
[21] M. Gäckle, D. Merten, Modelling the temporal intensity distribution in laser ablation-inductively coupled plasma-mass spectrometry (LA-ICP-MS) using scanning and drilling mode, Spectrochim. Acta Part B 60 (2005) 1517–1530.
[22] J. Koch, G. Schaldach, H. Berndt, K. Niemax, Numerical simulation of aerosol transport in atomic spectrometry, Anal. Chem. 76 (2004) 130A–136A.
[23] D. Bleiner, A. Bogaerts, Computer simulations of laser ablation sample introduction for plasma-source elemental microanalysis, J. Anal. At. Spectrom. 21 (2006) 1161–1174.
[24] D. Bleiner, A. Bogaerts, Computer simulations of sample chambers for laser ablation-inductively coupled plasma spectrometry, Spectrochim. Acta Part B 60 (2007) 155–168.
[25] C.C. Garcia, H. Lindner, K. Niemax, Transport efficiency in femtosecond laser ablation inductively coupled plasma mass spectrometry applying ablation cells with short and long washout times, Spectrochim. Acta Part B 62 (2007) 13–19.
[26] E.L. Gurevich, R. Hergenröder, A simple laser ICP-MS ablation cell with wash-out time less than 100 ms, J. Anal. At. Spectrom. 22 (2007) 1043–1050.
[27] D. Günther, C.A. Heinrich, Enhanced sensitivity in laser ablation-ICP mass spectrometry using helium–argon mixtures as aerosol carrier, J. Anal. At. Spectrom. 14 (1999) 1363–1368.
[28] D. Bleiner, H. Altorfer, A novel gas inlet system for improved aerosol entrainment in laser ablation inductively coupled plasma mass spectrometry, J. Anal. At. Spectrom. 20 (2005) 754–756.
[29] I. Prigogine, Irreversibility and randomness, Astrophys. Space Sci. 65 (1979) 371–381.
[30] I. Prigogine, Chaotic Dynamics and Transport in Fluids and Plasmas, AIP Press, 1993.
[31] W.D. McComb, The Physics of Fluids Turbulence, Oxford University Press, 1992.
[32] B.P. Leonard, Turbulence and its Simulation, Springer, 1992.
[33] D.C. Wilcox, Turbulence modelling for CFD, DCW Industries, 1992.
[34] B.E. Launder, D.B. Spalding, The numerical computation of turbulent flows, Comput. Methods Appl. Mech. Eng. 3 (1974) 269–289.
[35] B.E. Launder, Second moment closures: present and future? Int. J. Heat Fluid Flow 10 (1989) 282–300.
[36] T.-H. Shih, W.W. Liou, A. Shabbir, Z. Yang, J. Zhu, A New k–ε eddy–viscosity model for high Reynolds number turbulent flows — model development and validation, Comput. Fluids 24 (1995) 227–238.
[37] W. Rodi, N. Fueyo, Engineering Turbulence Modelling and Experiments 5, Elsevier Science, 2002.
[38] U. Schumann, Realizability of Reynolds stress turbulence models, Phys. Fluids 20 (1977) 721–725.
[39] Q.Q. Lu, J.R. Fontaine, G. Aubertin, A Lagrangian model for solid particles in turbulent flows, Int. J. Multiph. Flow 19 (1993) 347–367.
[40] D. Günther, J. Koch, private communication.
[41] W.C. Hinds, Aerosol Science and Technology, Wiley, 1999.
[42] P. Baron, K. Willeke, Aerosol Measurement:Principles, Techniques and applications, Wiley–Interscience, 2001.
[43] C. He, G. Ahmadi, Particle deposition in a nearly developed turbulent duct flow with electrophoresis, J. Aerosol Sci. 30 (1999) 739–758.
[44] A. Li, G. Ahmadi, Deposition of aerosols on surfaces in turbulent channel flow, Int. J. Eng. Sci. 31 (1993) 435–451.
[45] P.G. Saffman, The lift force on a small sphere in a slow shear flow, J. Fluid Mech. 22 (1965) 385–400.
[46] H. Ounis, G. Ahmadi, Analysis of dispersion of small spherical particles in a random velocity field, J. Fluids Eng. 112 (1990) 114–120.
[47] J. Koch, A. von Bohlen, R. Hergenröder, K. Niemax, Particle size distributions and compositions of aerosols produced by near-IR femto- and nanosecond laser ablation of brass, JAAS 19 (2004) 267–272.
[48] J. Koch, H. Lindner, A. von Bohlen, R. Hergenröder, K. Niemax, Elemental fractionation of dielectric aerosols produced by near-infrared femtosecond laser ablation of silicate glasses, J. Anal. At. Spectrom. 20 (2005) 901–906.
[49] H. Lindner, Untersuchungen zur Partikelverteilung und-zusammensetzung beim Laserabtrag, Diploma thesis, University of Dortmund, 2004.
[50] L.B. Loeb, The kinetic theory of gases, Dover Publications, 1961.
[51] R.C. Reid, J.M. Prausnitz, B.E. Poling, The properties of gases and liquids, McGraw–Hill, 1987.
[52] P. Rosin, E. Rammler, The laws governing the fineness of powdered coal, J. Inst. Fuel 7 (1933) 29–36.
[53] Z. Chen, D. Bleiner, A. Bogaerts, Effect of ambient pressure on laser ablation and plume expansion dynamics: a numerical simulation, J. Appl. Phys. 99 (2006) 1–9 063304.
[54] Z. Chen, A. Bogaerts, Laser ablation of Cu and plume expansion into 1 atm ambient gas, J. Appl. Phys. 97 (2005) 1–11 063305.
[55] C.C. Garcia, W. Wälle, H. Lindner, J. Koch, K. Niemax, D. Günther, Femtosecond laser ablation inductively coupled plasma mass spectrometry: Transport efficiencies of aerosols released under argon atmosphere and the importance of the focus position, Spectrochim. Acta Part B 63 (2008) 271–276, doi:10.1016/j.sab.2007.11.017.
[56] unpublished data.
[57] L. Halicz, D. Günther, Quantitative analysis of silicates using LA-ICP-MS with liquid calibration, J. Anal. At. Spectrom. 19 (2004) 1539–1545.
[58] J. Pisonero, D. Fliegel, D. Günther, High efficiency aerosol dispersion cell of laser ablation-ICP-MS, J. Anal. At. Spectrom. 21 (2006) 922–931.